The Identification of Hydrogen Trapping States in an Al-Li-Cu-Zr Alloy Using Thermal Desorption Spectroscopy

STEPHEN W. SMITH and JOHN R. SCULLY

Thermal desorption spectroscopy (TDS) was utilized to identify several metallurgical states in an Al - 2Li - 2Cu-0.1Zr (wt pct) alloy, which trap absorbed hydrogen. Six distinct metallurgical desorption states for hydrogen were observed for tempers varying from the T3 to peakaged condition. Lower energy thermal desorption states were correlated with interstitial sites, lithium in solid solution, and δ' (Al_3Li) precipitates. These states have trap-binding energies $\leq$25.2 kJ/mol. Under the charging conditions utilized, approximately 4 pct of the total (*e.g.*, trapped and lattice) hydrogen content was associated with interstitial sites, consistent with the view that the intrinsic lattice solubility of hydrogen in aluminum is very low. In contrast, dislocations, grain boundaries, and T_1 (Al_2CuLi) particles were found to be higher energy-trap states with trap-binding energies $\geq$31.7 kJ/mol. Approximately 78 pct of all absorbed hydrogen occupied these states. Moreover, greater than 13 pct of the available trap sites at grain boundaries were occupied. Such a high hydrogen coverage at grain-boundary sites supports the notion that hydrogen contributes to grain-boundary environmental cracking in Al-Li-Cu-Zr alloys. Also, it points out the error in assuming that hydrogen cannot play a major role in cracking of Al-based alloys due to the low lattice solubility.

I. INTRODUCTION

Al-Li-Cu-Zr alloys have been shown to be susceptible to environmentally assisted cracking (EAC) when exposed to aqueous chloride-containing environments.[1–4] However, there has been little research to distinguish dissolution-based processes from hydrogen-embrittlement processes for this system. For instance, the presence of T_1 in Al-Li-Cu-Zr alloys has been argued to result in both aqueous dissolution and hydrogen embrittlement under similar conditions.[5] However, the role of T_1 in each of these processes has not been isolated. For Al-Li-Cu-X alloys, intergranular, intersubgranular, and transgranular EAC paths in aqueous solutions have been attributed to boundary-T_1 dissolution,[6] T_1 dissolution with hydrogen uptake,[7] $AlLiH_4$ formation and cracking,[8,9] dissolution of copper-depleted zones,[10] and intrinsic hydrogen embrittlement involving mobile and or trapped hydrogen.[11] Which of these or other metallurgical factors control hydrogen-assisted cracking has not been clearly established. Consequently, knowledge of important factors controlling EAC and governing mechanisms are not available.

To gain insight on the interaction of absorbed hydrogen with Al-Li-Cu-Zr alloys, electrochemically precharged specimens were examined by an ultra-high-vacuum gas extraction technique, thermal desorption spectroscopy (TDS). Thermal desorption spectroscopy has been used to measure the binding energies of surface-adsorbed species since the mid-1950s.[12,13,14] This technique was not applied to the analysis of species that were absorbed in the bulk of a material and trapped at microstructural sites of varying binding energy until the early 1980s.[15,16] When this technique is used to measure bulk-absorbed species, detrapping and lattice diffusion must precede surface desorption. As the temperature of a sample is increased, the rate of gas evolution will increase, resulting in an instantaneous rise in gas density within a fixed volume. If a mass spectrometer is used to measure the rise of pressure within the chamber, the flux of any desorbed species can be determined. It is this ability to dynamically measure evolved gases and to discriminate the evolved species that makes this tool more powerful than traditional fusion methods used to determine the total concentration of absorbed species.[17]

To fully understand the process of hydrogen embrittlement, one must establish a fundamental understanding of the ingress, transport, and trapping of hydrogen in a material system.[18,19] This article serves as a first step to developing such an understanding. With this information, a more accurate assessment of the effect of absorbed hydrogen on the mechanical behavior of these alloys can be developed.[20]

II. EXPERIMENTAL

A. *Materials*

Several alloys were used to determine the active hydrogen-trapping sites in Al-Li-Cu-Zr alloys. These alloys varied in composition, which results in a variation of precipitation phases, and contained various concentrations of defect sites, which may act as hydrogen-trapping sites. Three different Al-Li-Cu-Zr alloys were used in this study. The first alloy was a commercially available, 3.2-mm-thick, AA2090 (Al - 2.15Li - 2.56Cu - 0.12Zr, wt pct), unrecrystallized sheet product. The two other Al-Li-Cu-Zr alloys were recrystallized alloys fabricated from the same plate, whose composition (Al - 2.05Li - 2.27Cu - 0.09Zr, wt pct) was within nominal limits for the AA2090 designation.[21] Following hot rolling of the plate, these alloys were heated at different

STEPHEN W. SMITH, formerly Graduate Research Assistant, Department of Materials Science and Engineering, University of Virginia, Charlottesville, VA 22903, is Senior Engineer, Lockheed Martin Engineering and Sciences, Hampton, VA 23681-2199. JOHN R. SCULLY, Associate Professor, is with the Department of Materials Science and Engineering, University of Virginia, Charlottesville, VA 22903.

Manuscript submitted March 9, 1998.

Table I. Grain Dimensions of the Three Al-Li-Cu-Zr Alloys Examined

Alloy	Product Form	Recrystallization Heating Rate (°C/h)	Grain Dimensions (μm) (L × LT × ST)	Subgrain Dimensions (μm)
AA2090	unrecrystallized	—	4400 × 600 × 10	5 to 10
Al-Li-Cu-Zr	recrystallized fine grain	700,000	30 × 30 × 20	—
Al-Li-Cu-Zr	recrystallized large grain	70	1200 × 1100 × 250	—

Table II. Strengthening Precipitates in Commercial Al-Li-Cu-Zr Alloys[36,37,47]

Precipitate	Composition	Morphology	Orientation	Coherency	Nucleation	Crystal Structure	Comments
δ'	Al_3Li	spheres	cube-cube	fully	homogeneous	$L1_2$	metastable phase of δ; found in naturally aged condition, will coarsen with artificial aging; δ can be formed at high angle boundaries upon significant aging
T_1	Al_2CuLi	plates	{111} habit	partially	dislocations, subgrain boundaries	hexagonal	little to none found in naturally aged condition, will nucleate and coarsen with artificial aging; $T_2(Al_6Cu(Li,Mg)_3)$ and $T_B(Al_7Cu_4Li)$ can also be formed at high angle grain boundaries with significant aging
θ'	Al_2Cu	plates	{001} habit	partially	subgrain boundaries	tetragonal	grows at the expense of GP_{ZONES}, metastable phase of θ, found in naturally aged condition; only observed for Cu:Li > 1:3

rates in a recrystallization treatment, to develop distinct grain sizes in each alloy.[22] Following recrystallization, the alloys were solution heat treated at 545 °C for 1 hour, quenched, and stretched to a total of 6 pct plastic engineering strain (this was the same total stretch level as used in the commercial AA2090 product). Microstructural characterization was performed using optical, scanning electron, and transmission electron microscopy (TEM) for each alloy. Selected area diffraction patterns and centered dark-field images were employed to aid in phase identification. The two recrystallized alloys and the commercial unrecrystallized alloy varied dramatically in grain size (Table I). Additionally, the unrecrystallized alloy contained a subgrain structure, on the order of 5 to 10 μm, which was not present in the recrystallized products. Each alloy was examined in three different tempers, the naturally aged (T3) condition, an underaged (T3 + 5 h at 160 °C), and a peakaged (T3 + 25 h at 160 °C) temper. The size and density of precipitate phases are altered by the aging conditions and stretch level prior to aging.[23] The strengthening precipitates which are most often encountered in commercial Al-Li-Cu-Zr alloys are listed in Table II.

Several binary alloys (Al - 1Cu, Al - 4Cu, and Al - 3Li, wt pct) were also used to aid in hydrogen-trap-site identification. These binary alloys enable separate investigation of hydrogen interactions with copper-rich (Guinier–Preston zones, θ'', θ' and θ) and lithium-rich (δ' and δ) phases. The binary products were sectioned to a thickness of 1.2 mm. Whenever a direct comparison between the desorption behavior of an Al-Li-Cu-Zr alloy was made with one of the binary alloys, the Al-Li-Cu-Zr alloy was also thinned to 1.2 mm, to ensure a comparable diffusion distance for the desorbing species.

B. *Hydrogen Charging Procedures*

Prior to hydrogen charging, the front and back faces of each specimen were treated to minimize native-aluminum-oxide-film growth, which can reduce hydrogen absorption. This procedure involved vacuum etching the native oxide followed by the deposition of a thin nickel film, which is thermodynamically stable and will not hydride under the charging conditions utilized. Specimens measuring approximately 12.7 × 25.4 mm were dry ground, using SiC paper to a final grit of 1200. The final thickness of each specimen was either 1.2 or 2.4 mm. Polished specimens were placed in a very-high-vacuum sputtering chamber and evacuated to less than 2.7×10^{-5} Pa (2.0×10^{-7} Torr). The system contained a liquid nitrogen cold finger, to aid in water vapor condensation from the vacuum environment. Specimens were etched at 350 V and 0.8 mA/cm^2 in a 2.4 Pa Ar (99.999 pct) environment for 8 minutes, using an RF power supply. The field was then reversed and a shield retracted, to facilitate sputter deposition from a high-purity nickel (99.999 pct) target spaced approximately 15 cm from the substrate. Sputtering was performed at 600 V and 0.6 mA/cm^2 in a 2.4 Pa Ar (99.999 pct) environment for 5 minutes. Following nickel deposition on one face of the specimen, the chamber was opened and the specimen was rotated to expose the opposite face. The etching and deposition procedures were then repeated for the opposite face of the specimen. This

procedure produced a nickel film of approximately 400 Å, as measured on separate samples using a surface roughness tester with a diamond tip stylis, on the front and back face of each specimen. The nickel film on each face made it possible to electrochemically charge both faces of the specimen simultaneously. The diffusivity of hydrogen in aluminum oxide is several orders of magnitude lower than in pure aluminum.[24] Therefore, the oxide can act as a diffusion barrier. The etching and deposition procedures were used to minimize the native-oxide diffusion barrier.

Electrochemical charging of the nickel-coated specimens was performed in a 0.25 M Na_2SO_4 + 0.05 M sodium borate solution buffered to a pH of 7 with boric acid under potentiostatic control at -1 V_{SCE} for 28 days ($f_{H_2} \approx 2 \times 10^{11}$ atm). The relatively long charging period was required to increase the concentration of absorbed hydrogen through the thickness of the Al-Li-Cu-Zr specimens, due to the slow hydrogen diffusivity in aluminum alloys (approximately 1×10^{-13} m^2/s[25,26]). After charging, specimens were removed from solution and examined optically to ensure the nickel films were not pitted. Prior to thermal desorption analysis, specimens were dry ground with 800 grit SiC paper, to remove the nickel film, and cleaned in methanol. It should be noted that this charging procedure did not produce a completely uniform hydrogen concentration through the specimen thickness, particularly for the 2.4-mm-thick specimens. However, this procedure was determined to result in increased hydrogen concentrations. The relevance of using specimens which are not uniformly charged will be addressed within the text.

Straining electrode tests (SET) were also performed to study the ingress of hydrogen in AA2090 under dynamic straining. Flat, 2.4-mm-thick tensile samples (L oriented) were preloaded to 75 pct σ_{ys} and strained at a constant crosshead displacement rate (5×10^{-5} mm/s) with an initial strain rate of 2×10^{-6} s^{-1}. The preloaded samples, which did not have a protective nickel film, were exposed to a pH 1 solution (0.1 M HCl) and held at a potential of -2 V_{SCE}, while being strained to a total engineering strain of 3 pct, following the procedures of Albrecht and co-workers.[27] The solution chemistry and charging potential were chosen to ensure the water-reduction reaction and to minimize oxidation of the specimens while chemically destabilizing the passive film to promote hydrogen uptake. After the SET was performed, the tensile specimen was removed from solution, the gage section was removed using a diamond wafering blade, and was then prepared for thermal desorption analysis in the same manner as the Ni-coated hydrogen-precharged specimens (*i.e.*, dry ground and cleaned).

C. *Thermal Desorption Spectroscopy*

The thermal desorption system used for this work is shown in Figure 1. The vacuum system is comprised of two sections; below the gate valve is the ultra-high-vacuum (UHV) analysis section, and above the gate valve is a high-vacuum, load-lock section to permit sample insertion while maintaining UHV in the analysis section. All tubular components within the UHV system have ConFlat metal-to-metal seals which can be repeatedly baked to 450 °C to aid in cleaning the system of adsorbed species. The analysis section is pumped by a 180 L/s (N_2) turbo-molecular pump (TMP) with a four-stage-diaphragm backing pump, in parallel with a 20 L/s (N_2)

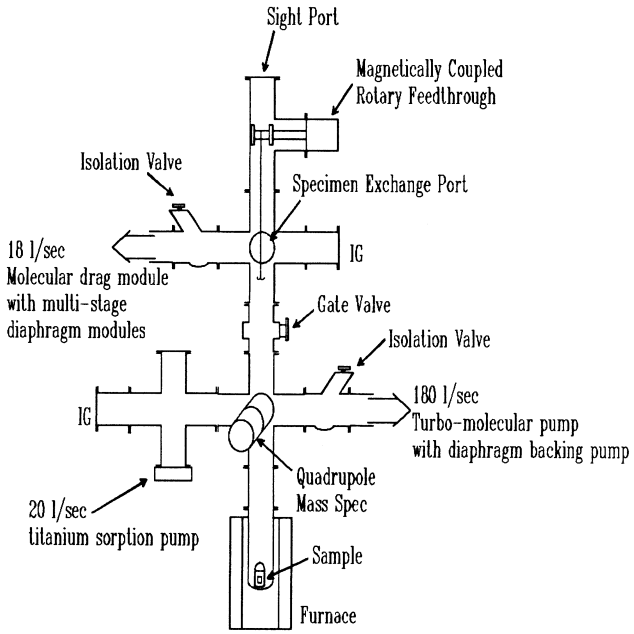

Fig. 1—Schematic diagram of TDS system.

titanium sorption pump (TSP), which provides an ultimate pressure in the low 10^{-10} Pa range ($\approx 10^{-12}$ Torr). The specimen-exchange section is pumped using an 18 L/s (N_2) molecular drag pump with a diaphragm-module backing pump, producing an ultimate pressure in the low 10^{-3} Pa range ($\approx 10^{-5}$ Torr). Specimen heating was provided by a resistance tube furnace capable of heating a specimen above 900 °C at a linear heating rate with a programmable controller. The control element for the furnace is a thermocouple located within the vacuum chamber in close proximity to the specimen. Measured temperatures were determined to be within 3 °C of the specimen temperature at 600 °C. During specimen heating, a quadrupole mass spectrometer (QMS) was used to measure the hydrogen partial pressure within the analysis section.

Specimens to be analyzed were loaded into a prebaked quartz crucible suspended from the rotary feedthrough. The exchange section was evacuated to 2.6×10^{-2} Pa (2×10^{-4} Torr), the gate valve opened, and the specimen lowered to the bottom of the quartz tube located within the furnace. The exchange section was then closed and the TSP operated to more effectively pump water vapor and hydrogen from the system. An adequate vacuum was established ($< 2.6 \times 10^{-7}$ Pa, $< 2 \times 10^{-9}$ Torr), prior to desorption experiments. To ensure a constant pumping speed during thermal desorption, the TSP was turned off and the isolation valve leading to the turbo-molecular pump was partially closed to a fixed position. This resulted in a hydrogen pumping speed of 8.31 L/s from the analysis chamber.[28] During each hydrogen-analysis test, the signals of selected mass-to-charge ratios and the specimen temperature were recorded as a function of time. When possible, duplicate desorption tests were performed to ensure that the results were reproducible. Generally, there were slight variations in the desorption spectra for specimens that were hydrogen charged under the same conditions. However, the total hydrogen desorbed from specimens that were Ni coated and hydrogen precharged was very consistent (± 2.5 pct). Additionally, curve-fitting has

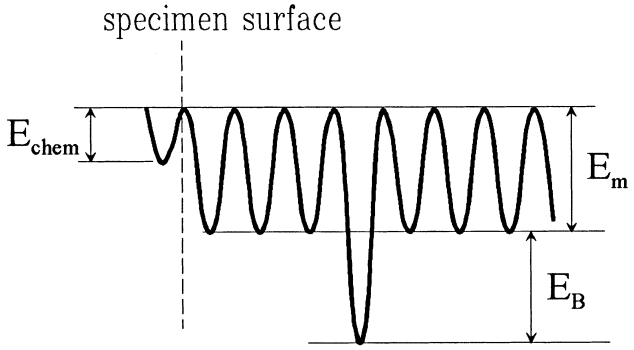

Fig. 2—Potential energy diagram depicting the detrapping, diffusion, and desorption of an absorbed species.

shown that the hydrogen trapped at each state was very reproducible for specimens prepared in the same manner.

D. *Desorption Rate Analysis*

The flux of a gaseous species during thermal desorption can be determined by measuring the change in partial pressure of a species within a vacuum vessel of known volume. A mass balance is used to determine the desorption rate of absorbed species.[29] The desorption rate for any species can be determined by measuring the partial pressure within the analysis volume.[28] For a chamber of fixed volume and hydrogen pumping speed,

$$(F_d)_{\mathrm{H}_2} = \left(V \frac{dp_{\mathrm{H}_2}}{dt} \right) + (F_p)_{\mathrm{H}_2} \qquad [1]$$

where F_d is the desorption rate from the specimen, V is the volume of the analysis chamber, p_{H_2} is the hydrogen partial pressure, and F_p is the pumping rate of the turbo-molecular pump.

For the case of hydrogen trapped within the bulk of a metal sample, the rate of desorption can be evaluated using the rate equations governing three distinct processes. The detrapping, diffusion, and desorption of hydrogen are thermally activated during thermal desorption analysis. A schematic representing the activation energy for each of these processes is shown in Figure 2. Each of these processes can be expressed by an Arrhenius equation

$$\frac{k_d}{k_t} = \gamma \exp\left(-\frac{E_B}{\mathrm{k}T} \right) \text{ detrapping} \qquad [2]$$

$$D_{\mathrm{H}} = D_{\mathrm{o}} \exp\left(-\frac{E_m}{\mathrm{k}T} \right) \text{ lattice diffusion} \qquad [3]$$

$$\frac{k_{\mathrm{des}}}{k_{\mathrm{ads}}} = A \exp\left(-\frac{E_{\mathrm{chem}}}{\mathrm{k}T} \right) \text{ desorption} \qquad [4]$$

where k_d, k_t, k_{des}, and k_{ads} are the rate constants for detrapping, trapping, desorption, and adsorption, respectively. The pre-exponential terms γ and A account for the change in free energy of hydrogen during the respective processes. The term γ can be expressed as[30]

$$\gamma = \frac{Z_d \nu_d \exp\left(\frac{S_d}{k} \right)}{Z_t \nu_t \exp\left(\frac{S_t}{k} \right)} \qquad [5]$$

where Z_d and Z_t are the coordination numbers for hydrogen in an interstitial and a trapping site, ν_d and ν_t are the vibrational frequencies, and S_d and S_t are the entropies of detrapping and trapping, respectively. Because the free energy of a hydrogen atom does not change during the migration from interstitial site to interstitial site, the pre-exponential term D_{o} is a material constant. Outlaw and co-workers[31] and Anyalebechi[32] demonstrated the energy of chemisorption for hydrogen on selected aluminum alloys, including aluminum-lithium binaries,[32] is relatively low compared to the migration energy for hydrogen. Therefore, the thermally activated surface desorption of hydrogen can be neglected in the derivation of the net desorption rate for trapped hydrogen for many aluminum alloys.

Ono and Meshii[30] developed a solution for the net desorption of hydrogen from a bulk specimen considering the rates of detrapping (Eq. [2]) and diffusion (Eq. [3]) as the rate-controlling processes. However, they did not include a term for the available interstitial sites present in the material. The detrapping process can be expressed in terms of hydrogen atoms and available occupation sites.

$$\mathrm{H}_L + \square_T \underset{k_d}{\overset{k_t}{\leftrightarrow}} \mathrm{H}_T + \square_L \qquad [6]$$

where H_L and H_T represent a hydrogen atom at a lattice interstitial site and a trap site, respectively, and $\square_T$ and $\square_L$ represent a vacant trap site and interstitial site, respectively. The rate constants for trapping and detrapping can then be used to yield

$$\frac{k_t}{k_d} = \frac{C_T N_L}{C_L N_T} \quad \text{or} \quad \frac{C_T}{C_L} = \frac{k_t N_T}{k_d N_L} \qquad [7]$$

where C_L and C_T are the lattice hydrogen and trapped hydrogen concentrations (atoms H/cm^3), and N_{L} and N_{T} are the available lattice interstitial sites and available trap site concentrations (sites/cm^3), respectively. This rate equation can now be used to account for the effect of trapping sites on the diffusivity of hydrogen.

$$D_e = D_{\mathrm{H}} \frac{C_L}{C_L + C_T} = D_{\mathrm{H}} \left(1 + \frac{k_t N_T}{k_d N_L} \right)^{-1} \qquad [8]$$

where D_e is the effective diffusivity. Using this controlling-rate equation, Ono and Meshii assigned boundary conditions for a semi-infinite plate of thickness $2d$ being heated at a constant thermal ramp rate ($d\mathrm{T}/dt$). These conditions allow for an approximate desorption rate equation to be expressed as

$$\frac{\partial C_L}{\partial t} = -\alpha^2 D_e (C_{\mathrm{H}} - C_{\mathrm{o}}) \qquad [9]$$

where C_{H} is the total hydrogen concentration, C_{o} is the thermal equilibrium concentration of hydrogen, and α is the lowest order eigenvalue that satisfies the prescribed boundary conditions ($\alpha = \pi/2d$). Due to the low hydrogen partial pressure within the vacuum chamber used for thermal

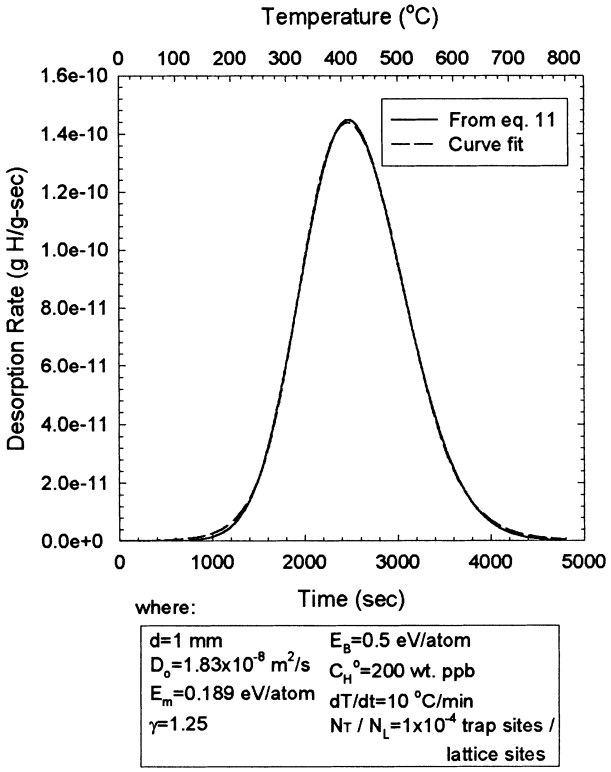

Fig. 3—Model desorption rate curve developed using Eq. [11].

desorption, C_o will be much lower than the total hydrogen concentration of the material being studied and will, therefore, be assumed to be zero.

Substituting Eq. [8] into [9] and rewriting this equation to express it in terms of a change in the lattice concentration (C_L) over some incremental time over which the temperature change is small enough to be approximated as constant yields

$$\frac{\Delta C_L}{\Delta t} = \alpha^2 D_{\mathrm{H}} \left(1 + \frac{k_t N_T}{k_d N_L}\right)^{-1} (C_{\mathrm{H}}) \qquad [10]$$

Using Eq. [2], [3], and [6], Eq. [10] can be modified.

$$\frac{\Delta C_L}{\Delta t} = \left(\frac{\pi}{2d}\right)^2 D_{\mathrm{o}} \exp\left(-\frac{E_m}{\mathrm{k}T}\right) \left(1 + \frac{1}{\gamma}\left(\frac{N_T}{N_L}\right) \exp\left(\frac{E_B}{\mathrm{k}T}\right)\right)^{-1} (C_{\mathrm{H}}) \qquad [11]$$

Equation [11] can be used to model the desorption of bulk absorbed hydrogen from multiple trapping sites of a constant binding energy. If appropriate values are used, a model desorption-rate-*vs*-time curve can be generated (Figure 3). This curve is a Gaussian curve which is skewed to the left. The shape of this curve is indicative of a rate order which is between first and second order.[13,29] A rate order between first and second order has been attributed to a first order detrapping process that is affected by diffusion.[13]

To resolve the contribution of hydrogen detrapping from several trapping states, a nonlinear curve-fitting program, PEAKFIT,* was used to fit experimental data. This software package has a library of equations including an asymmetric double sigmoidal, which can be used to model the detrapping of hydrogen from a metallurgical trapping state (Figure 3). Curvefitting of total hydrogen-desorption-rate data can be used to identify the total number of distinguishable trapping states, as well as the amount of hydrogen that is trapped at each state.

It should be noted that the analysis which has been outlined within this section is not completely rigorous. Each trapping state is considered separately and there is no consideration for the potential retrapping of hydrogen by a trapping site after it has been detrapped from a site of different binding energy. It is particularly important to be aware of this fact when studying a material which contains multiple trapping states of similar binding energy.[48]

*PEAKFIT is a trademark of Jandel Scientific, Corte Madera, CA.

E. *Activation Energy Analysis*

The study of thermally activated processes by differential thermal analysis (DTA) has demonstrated that the position of a reaction rate maximum varies with heating rate if other experimental variables are fixed.[33] This behavior has also been demonstrated for the desorption of trapped hydrogen using TDS.[15] Most reactions of the type solid + absorbed specie → solid + gas can be described by the equation

$$\frac{dX}{dt} = A(1 - X)^n \exp\left(-\frac{E_{\mathrm{a}}}{\mathrm{k}T}\right) \qquad [12]$$

where dX/dt is the rate of reaction, X is the fraction reacted, A is a pre-exponential constant, and n is the empirical order of the reaction. Applying this single Arrhenius equation to the desorption of bulk hydrogen, the activation energy, E_a, is used to represent the total activation energy for desorption ($E_m + E_B$). This approach has been shown to be correct for thermal desorption analysis.[16]

Several researchers have modified this desorption equation to express the activation energy in terms of heating rate (dT/dt) and temperature for a desorption maxima (T_m).[16,33]

$$\frac{d\left(\ln \frac{dT/dt}{T_m^2}\right)}{d\left(\frac{1}{T_m}\right)} = -\frac{E_a}{k} \qquad [13]$$

Using this relationship, $\ln((dT/dt)/T_m^2)$ *vs* $(1/T_m)$ for each desorption maxima can be plotted for several different thermal ramp rates to produce a line with the slope $-E_a/k$. This analysis has been shown to apply to experimentally determined desorption data and has enabled the calculation of binding energies for metallurgical trapping states in steel.[15] It should be noted that Lee *et al.*[15] neglected any role of diffusion following detrapping. This is a reasonable approximation for the case of steel, where the migration energy (typically <6 kJ/mol) is much lower than the binding energy for reversible traps (≥48 kJ/mol). Consequently, the detrapping of hydrogen dominates the desorption process. In the case of Al-Li-Cu-X alloys, the migration energy is a significant fraction of the overall activation energy for hydrogen detrapping. As a result, the diffusion of hydrogen to the free surface cannot be neglected.

An alternative approach to determine the activation energy

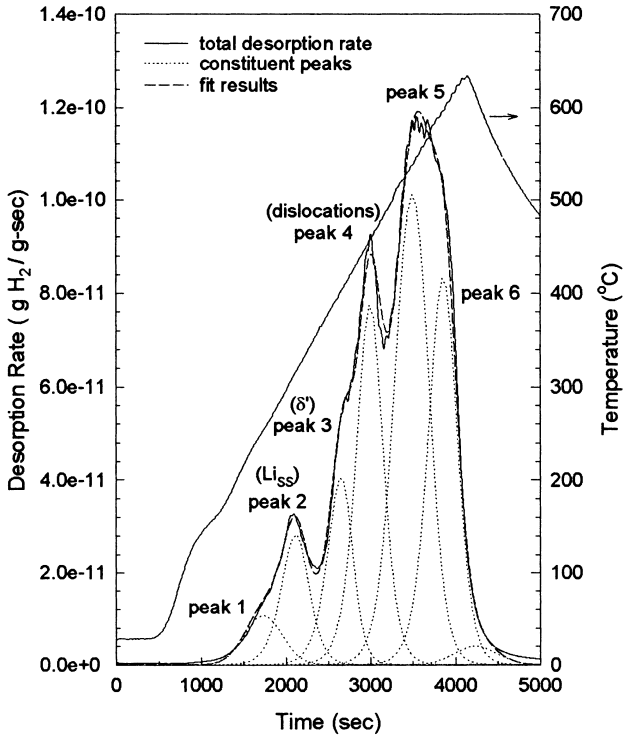

Fig. 4—Desorption spectra for AA2090, UA temper, tested at 10 °C/min. The desorption from each trapping state is shown using a fitted curve. Specimen is 2.4-mm thick and hydrogen precharged.

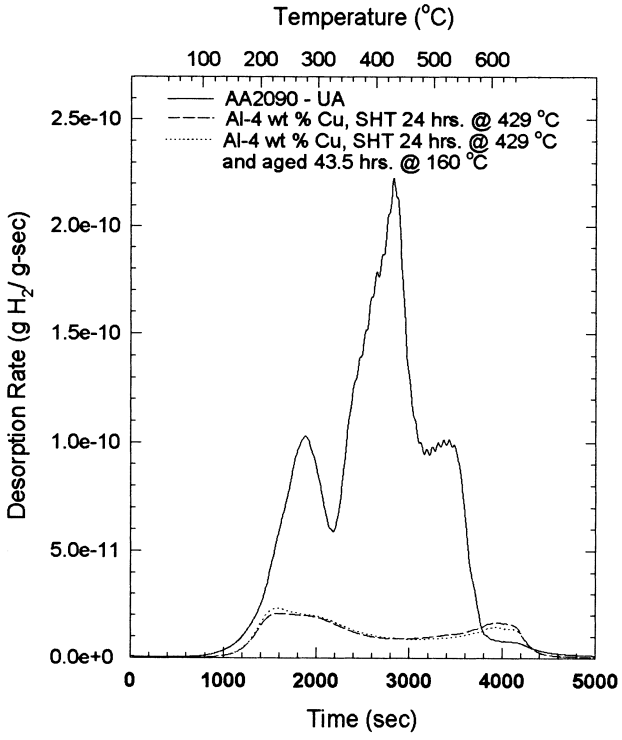

Fig. 5—Desorption spectra of AA2090, and Al-4 wt pct Cu, tested at 10 °C/min. All specimens are 1.2-mm thick and hydrogen precharged.

for the detrapping of hydrogen is the direct fitting of desorption-rate data for each trapping state, using Eq. [11]. This method does require the knowledge of several variables, such as the concentration of trap sites for the state being examined. In addition, the direct fitting of desorption-rate data from Eq. [11] requires a uniform hydrogen concentration through the thickness of each specimen, which is not the case in this study.

III. RESULTS

A. *Trap State Identification*

Figure 4 is a plot of the dynamic hydrogen desorption rate *vs* time for an electrochemically charged AA2090 UA specimen that was heated at 10 °C/min. In each of the three tempers examined, hydrogen was found to be trapped at six states. A seventh fitted curve, which is not identified, appears at the far right of the desorption curve in Figure 4. It was determined that this was associated with hydrogen desorption from the chamber walls *via* conduction heating. The identification of each trapping state was accomplished by comparing thermal desorption spectra for several model alloys which were hydrogen precharged. The tests that went into the identification of each trapping site will follow.

B. *Al-Cu Binaries*

The Al-1 wt pct Cu and Al-4 wt pct Cu alloys were tested under several aging conditions. These range from a solution-heat-treated state to a severely overaged condition. The desorption spectra for the Al-Cu binaries did not vary greatly as a function of aging, and the total hydrogen content was much lower than that in the AA2090 material under identical charging conditions (Figure 5). Because there are no significant changes in the trapping states associated with absorbed hydrogen upon aging, copper in solid solution and the copper-rich series of precipitates do not appear to act as significant sites for hydrogen trapping. These results correlate well with solubility measurements made by Anyalebechi.[34] Although he identified an increased hydrogen solubility in an Al-4 wt pct Cu alloy compared to pure Al, the total hydrogen solubility for each material was significantly lower than for an Al-3 wt pct Li binary and an AA2090 alloy.

C. *Al-Li Binaries*

The Al-3 wt pct Li binary alloy was examined in several different aging conditions. TDS analysis revealed two significant results: (1) the solubility of hydrogen in this alloy was much higher than in AA2090; and (2) three low-energy hydrogen-trap states contain varying amounts of hydrogen as a function of aging condition (Figure 6). Hydrogen solubility in Al-Li alloys has been shown to be strongly dependent upon Li content.[35] Therefore, a higher hydrogen concentration is expected in the Al-3 wt pct Li binary since it contains nearly 30 pct more Li than the AA2090.

The lowest energy-trapping state in the Al-Li binary alloy was significantly lower in energy than any trapping state found in AA2090. This low-energy trapping state contains a large amount of hydrogen in the solution-heat-treated condition. However, the total hydrogen associated with this state decreases sharply when aged (Figure 6). This trapping state appears to be hydrogen interacting with lithium on the free surface of the specimen or within the hydrated oxide layer. Hydrogen can be produced by the reduction of water vapor

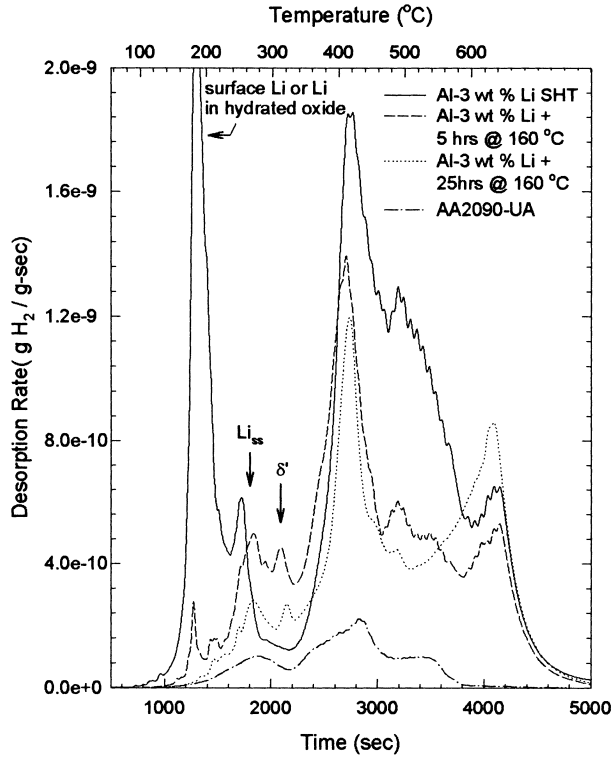

Fig. 6—Desorption spectra for Al-3 wt pct Li and AA2090, tested at 10 °C/min. All specimens are 1.2-mm thick and hydrogen precharged.

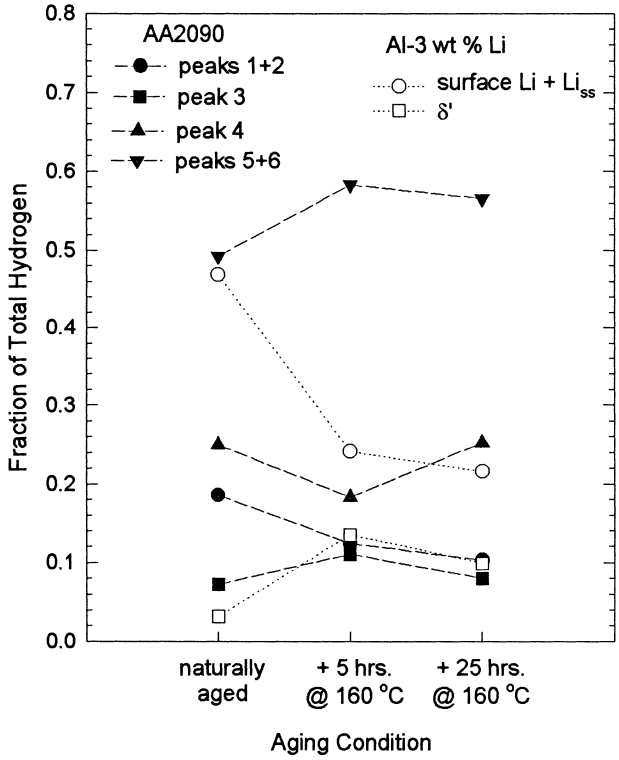

Fig. 7—Hydrogen partitioning for Al-3 wt pct Li and AA2090, tested at 10 °C/min. All specimens are 1.2-mm thick and hydrogen precharged.

in laboratory air as the specimen is prepared by dry grinding to an 800 grit finish. This effect was confirmed by testing uncharged specimens, which were prepared in the same manner. While the total amount of hydrogen desorbed was less than for the precharged material, the initial peak was still present and the amount of hydrogen desorbed from this state was not dependent upon the charging condition. Additionally, curve fitting of this trapping state was accomplished with a symmetric curve, indicative of a surface-controlled desorption process.[13] Therefore, this trapping state cannot be attributed to bulk absorbed hydrogen.

The second highest energy-trapping state identified for the Al-Li binary alloy was found to trap less hydrogen with aging. This trapping state was similar in energy and in its ability to trap hydrogen as a function of aging to the second trapping state identified for AA2090 (Figure 7). It appears that this trapping state is a result of hydrogen associated with lithium in solid solution. The total amount of hydrogen trapped by lithium in solid solution decreased with aging due to Li depletion from solid solution with the precipitation of Li-rich phases (δ' and δ in the Al-Li binary and δ' and T_1 for AA2090[36]).

The third trapping state observed in the Al-Li binary also varies with aging and behaves similarly to trapping state 3 for AA2090 (Figure 7). Only a small amount of hydrogen was associated with this third state before aging. Upon aging for 5 hours at 160 °C, the total hydrogen at this state increases. Further aging for 25 hours at 160 °C results in a decrease in hydrogen compared to 5 hours. However, it is higher than seen in the naturally-aged condition. Since the total amount of hydrogen associated with this state varied with aging, it is reasonable to assume that this trapping state correlates with the precipitation of δ' (Al_3Li). For AA2090 and the Al-Li binary, additional δ' is formed when artificially aged; upon further aging, some δ' is consumed with the formation of δ in the binary alloy and T_1 (Al_2CuLi) for AA2090. In both cases, the δ'-matrix interfacial area will be reduced as the δ' precipitates coarsen. This was shown to be the case for an experimental Al-Li-Cu-Zr alloy which was examined for several aging conditions.[37] It is not clear if the hydrogen associated with the coherent δ' precipitates will be trapped at the matrix (tensile) side of the matrix-particle interface due to the lattice mismatch between the lithium rich δ' particle and the aluminum-rich matrix (the lattice constant for δ' is more than 6 pct greater than for the matrix), or if the elevated hydrogen concentration will be present within the δ' particles due to the high concentration of lithium. However, the hydrogen concentration associated with δ' precipitates is much higher than would be observed in an aluminum-rich matrix without precipitates.

D. *AA2090*

To determine if dislocations can act as sites for hydrogen trapping, flat, tensile bars of AA2090 were plastically strained 3 pct prior to hydrogen charging to introduce an increased number of dislocations beyond the prestretch, thereby increasing the total number of potential trap sites along dislocations. Cathodic charging of these prestrained specimens resulted in an increased amount of hydrogen at trapping state 4 (Figure 8). Although prestraining these specimens will produce deformation bands which contain a very complicated dislocation structure, there do not appear to be any distinctly new trapping states created during deformation at this level. Accompanying the increase in trapped hydrogen

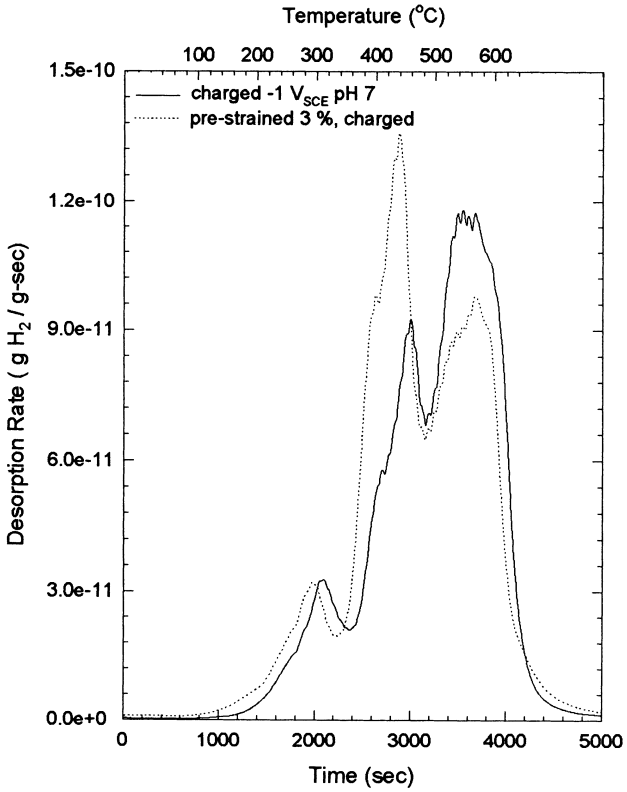

Fig. 8—Desorption spectra for AA2090, UA temper, in one case prestrained 3 pct in air, tested at 10 °C/min. Specimens are 2.4-mm thick and hydrogen precharged.

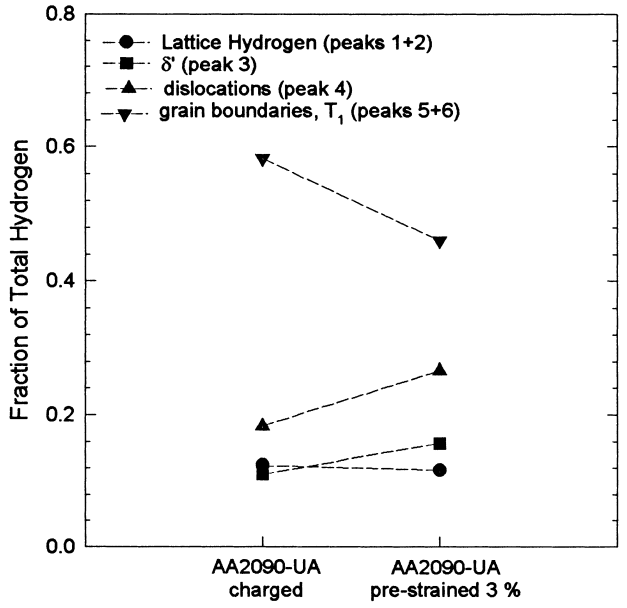

Fig. 9—Hydrogen partitioning of AA2090, UA temper, in one case prestrain 3 pct in air, tested at 10 °C/min. Specimens are 2.4-mm thick and hydrogen precharged.

at state 4 was a milder increase of hydrogen trapped at δ' particles, trap state 3 (Figure 9). This increase may be due to shearing of δ' particles by dislocations during plastic deformation,[38] thereby increasing the δ'-matrix interfacial area. For these two reasons, trapping state 4 has been

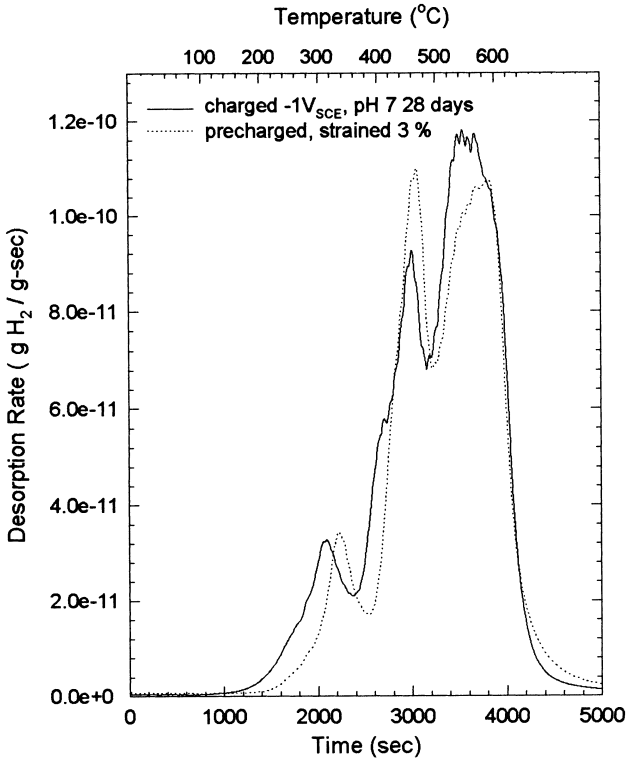

Fig. 10—Desorption spectra of AA2090, UA temper, in one case strained 3 pct, tested at 10 °C/min. Both specimens are 2.4-mm thick, Ni-coated, and precharged at −1 V_{SCE} for 28 days in pH 7 solution.

assigned to dislocations. The introduction of additional dislocation trapping sites resulted in a lowering of the effective diffusivity. By lowering the effective diffusivity, the rate of hydrogen ingress was reduced. Consequently, fewer of the high-energy trapping sites (peaks 5 and 6) in the interior of the specimen are exposed to the increased hydrogen concentration associated with charging. Additionally, a decreased diffusivity during charging also results in a decreased mean diffusion distance during desorption. This result can be observed as a shift in desorption maxima to lower temperatures.

Tensile specimens of the unrecrystallized alloy were strained at a constant crosshead displacement rate of 5×10^{-5} mm/s (initial strain rate of 2×10^{-6} s^{-1}) to a total engineering strain of 3 pct, following hydrogen charging. The gage area was sectioned from the tensile specimens and examined using TDS. Although these specimens were charged in the same manner as unstrained specimens, hydrogen desorption spectra for the strained gage volume are very different than for specimens which were not subject to any plastic deformation after hydrogen charging (Figure 10). While the total absorbed hydrogen remained constant, an increased fraction of hydrogen associated with trapping of hydrogen at dislocations was observed for deformed specimens (Figure 11). Additionally, there was a decrease in the total amount of hydrogen trapped at δ' precipitates, interstitially, and at solid-solution lithium atoms, along with a slight decrease in trapped hydrogen at states 5 and 6 subsequent to deformation. It appears that this repartitioning of internal hydrogen is due to dislocation generation and the pickup of hydrogen as dislocations sweep through the lattice. An additional effect may be due to a diffusional

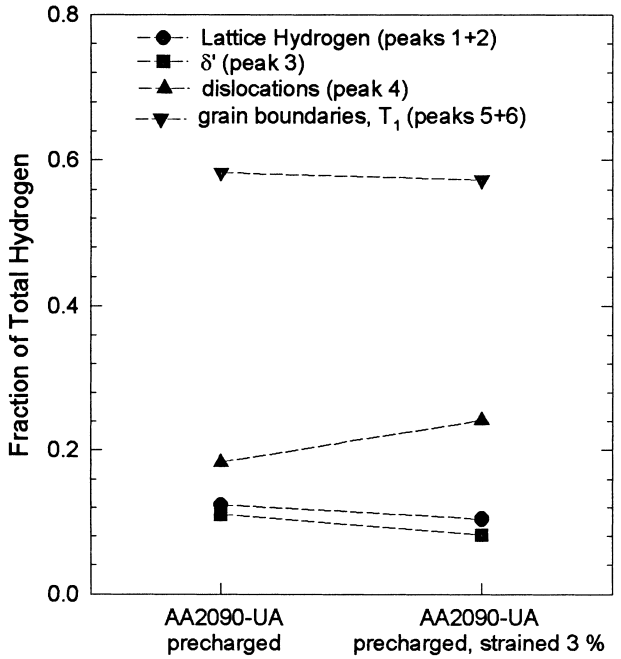

Fig. 11—Hydrogen partitioning of AA2090, UA temper, in one case strained 3 pct, tested at 10 °C/min. Both specimens are 2.4-mm thick, Ni-coated, and precharged at −1 V_{SCE} for 28 days in pH 7 solution.

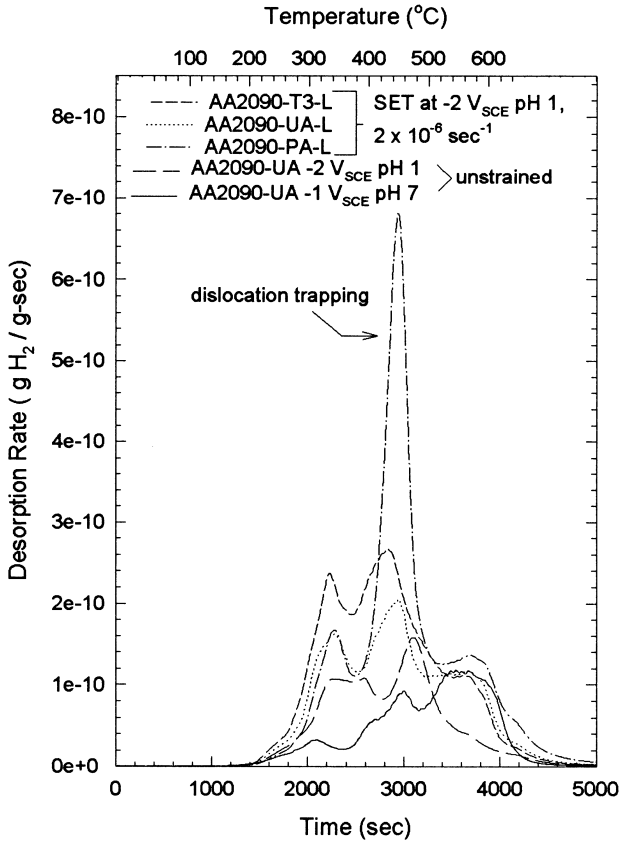

Fig. 12—Desorption spectra of AA2090, tested at 10 °C/min. Comparing 2.4-mm thick tensile specimens concurrently strained and charged in pH 1 HCl solution at −2 V_{SCE} to a total engineering strain of 3 pct to the Ni-coated and charged procedure.

process where the generation of dislocations creates additional trapping sites, and in order to minimize the free energy of the system, hydrogen atoms trapped at other states can diffuse to occupy the newly formed dislocation trapping sites.

Further evidence to support the redistribution of absorbed hydrogen by dislocations has been established by concurrent straining and cathodic charging using a straining electrode technique (SET). Following the concurrent straining and hydrogen charging of flat AA2090 (in the T3, underaged, and peakaged tempers) tensile specimens, the gage area was sectioned from the specimens and studied using TDS. In each of the tempers, the fraction of hydrogen trapped at dislocations (state 4) was significantly higher than measured in unstrained specimens using either the Ni-coated cathodic charging procedure or by charging a specimen in the pH 1 HCl solution used for the SET without dynamic straining (Figure 12). This effect was greatest in the PA temper, which has the highest degree of localized planar slip.[38] Additionally, the quantity of absorbed hydrogen was much higher for specimens subject to concurrent straining and cathodic charging than specimens charged in the same manner as the SET but without concurrent straining or specimens charged using the nickel-coated charging procedure. Therefore, dynamic straining increases the rate of hydrogen ingress in AA2090.

The peaks identified as trapping states 5 and 6 for AA2090 are very difficult to distinguish from one another. Release of hydrogen from state 6 occurs very close to the melting point. In order to avoid melting the aluminum specimens, the furnace was turned off approximately 20 °C below the melting point. If the specimen was allowed to melt, the desorption process would be different from the detrapping process which has been assumed. By comparing the total hydrogen released from precharged specimens heated in this manner with specimens which were heated beyond their melting point, it was determined that this alternate heating schedule (to approximately 640 °C) provides complete desorption of absorbed hydrogen from precharged AA2090 specimens. However, this does result in the desorption of hydrogen from specimens during a period of time in which the specimen is not being heated at a linear rate.

E. *Microstructural Alteration during TDS*

An inherent problem associated with TDS analysis is the potential to alter the microstructure of a specimen during heating. Artificial aging may produce new hydrogen trapping sites or result in the elimination of existing sites. If sites are eliminated, hydrogen desorption is a result of the elimination of sites and not the detrapping of hydrogen from these sites. For an initial assessment of the effect of specimen heating, several unrecrystallized AA2090 samples were heated at 10 °C/min and water quenched when various temperatures were reached. Vickers microhardness values were found to remain relatively constant for specimens heated to nearly 500 °C. For specimens heated above 500 °C, hardness values decreased with increasing temperature. Therefore, the microstructure is altered during the measurement of hydrogen desorption from states 5 and 6. Consequently, the desorption of hydrogen from states 5 and 6 may not represent the thermally activated detrapping of hydrogen. This may affect

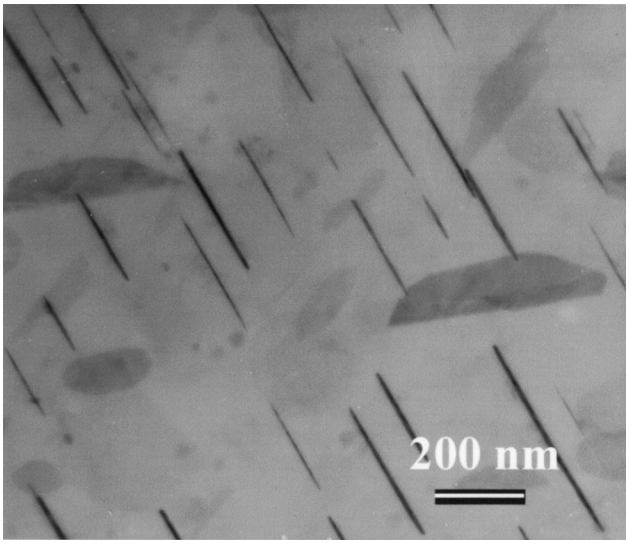

(*a*)

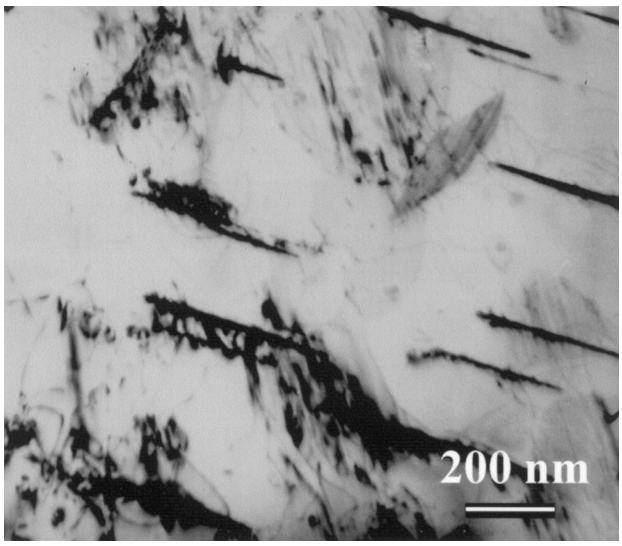

(*b*)

Fig. 13—Bright-field transmission electron micrographs of (*a*) unrecrystallized AA2090 UA temper and (*b*) unrecrystallized AA2090 UA temper heated to 450 °C at 10 °C/min. showing T_1 platelets in grain interiors.

curve fitting for these states as well as the evaluation of binding energies for these states.

The use of microhardness testing is a very coarse estimate of artificial aging. To more accurately determine potential aging below 500 °C, TEM was used to compare the microstructure of the unrecrystallized AA2090 in the UA temper with the same alloy heated to 450 °C at 10 °C/min and water quenched. The T_1 and T_2 platelets were not found to coarsen with thermal treatment and there was also no distinguishable change in platelet density (Figure 13). This was also true for T_B particles observed along high-angle grain boundaries. The dimensions of high-angle and subgrain boundaries also remained unchanged after heating up to 450 °C (Figure 14). Using TEM, it was not possible to determine the effect of heating on δ' precipitates. Therefore, differential scanning calorimetry (DSC) was used to examine any change for the unrecrystallized AA2090 alloy during thermal cycling. Figure 15 is a DSC trace for AA2090 in the UA temper

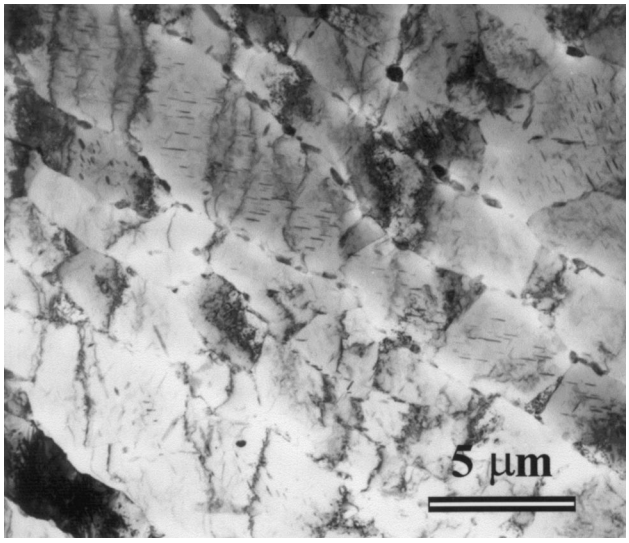

Fig. 14—Bright-field transmission electron micrograph showing subgrain boundary structure for unrecrystallized AA2090 UA temper heated to 450 °C at 10 °C/min.

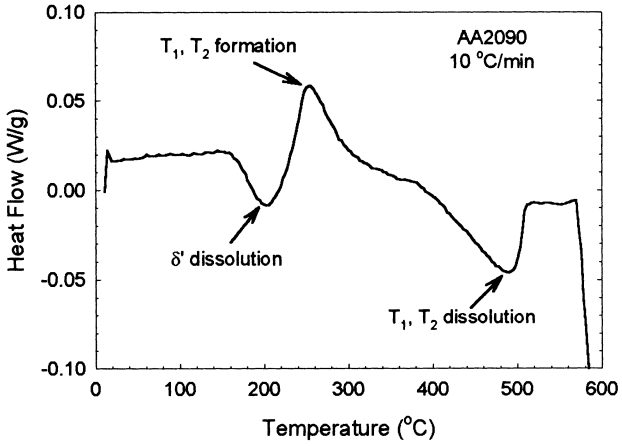

Fig. 15—DSC spectra for unrecrystallized AA2090 UA temper heated at 10 °C/min.

heated at 10 °C/min. The first peak identified is an endothermic peak at approximately 200 °C. This peak has been attributed to δ' dissolution.[39] The δ' desorption curve has been identified at a temperature greater than 200 °C (Figure 4). Therefore, this desorption curve may represent the release of hydrogen due to the elimination of δ' trapping sites. Two additional DSC maxima have also been identified; (1) an exothermic peak at approximately 260 °C which is associated with T_1 and T_2 formation; and (2) an endothermic peak at approximately 500 °C representing the dissolution of T_1 and T_2.[39] The presence of the peak at 500 °C is consistent with hardness measurements. However, the T_1 and T_2 formation exotherm is not consistent with the TEM micrographs shown in Figure 13. Since no obvious increase in T_1 or T_2 density was observed using TEM, the exothermic peak may represent only a small increase in the total T_1 and T_2 density.

F. *Recrystallized Al-Li-Cu-Zr*

Two recrystallized alloys of differing grain size (Table I) were cathodically charged under identical conditions and

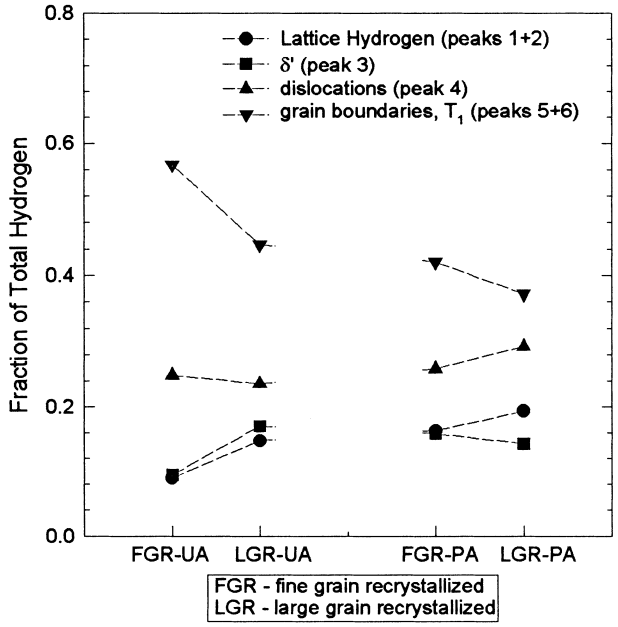

Fig. 16—Hydrogen partitioning of recrystallized Al-Li-Cu-Zr, tested at 10 °C/min. Specimens are 2.4-mm thick and hydrogen precharged.

studied using TDS. Independent of aging condition, the finer grain alloy contained a larger fraction of the total absorbed hydrogen at the high-energy trapping states (5 and 6) than did the coarser-grain alloy (Figure 16). Since the fine-grain alloy contains a higher density of grain-boundary sites, the trapping of hydrogen at high-angle grain boundaries will be increased as the grain size is decreased. These results indicate that one of the two high-energy trapping sites corresponds to hydrogen trapping at high-angle grain boundaries.

Analysis of the desorption spectra for the recrystallized alloys results in the observation of six trapping states. The recrystallized alloys, which do not contain subgrains, and the unrecrystallized alloy, which does contain subgrain boundaries, have the same number of active trapping states. Therefore, low-angle grain boundaries in and of themselves do not appear to provide effective hydrogen trapping sites in AA2090.

G. *Indirect Identification of Remaining Trapping States*

The second high-energy trapping state (5 or 6) must also be identified. Because this state has a high binding energy, it is believed to be either trapping at a precipitate or void, or the decomposition of a hydride phase. Other researchers have reported the existence of a hydride phase in Al-Li-Cu alloys when cathodically charged with hydrogen.[8,9] If the final high-energy site were due to the decomposition of a hydride phase, the amount of hydrogen released would have to be larger than seen in peak 5 or 6. For instance, if one of the high-energy trap sites were assumed to be $AlLiH_4$, the total hydrogen released from either of these states in a hydrogen-charged AA2090 specimen in the UA temper would correspond to less than 7×10^{-7} wt fraction (less than 6×10^{-6} vol fraction), which is significantly lower than has been reported.[8,9] Birnbaum *et al.*[40] have reported the introduction of hydrogen-vacancy traps in cathodically charged aluminum specimens. Comparison of TDS data for as-received and cathodically-charged AA2090 has not shown the introduction of a new trapping state with cathodic charging. Therefore, the hydrogen-vacancy interactions reported by Birnbaum and co-workers do not appear to be present for the conditions studied in this work. However, it is possible that the desorption of hydrogen from vacancies may be masked by a larger desorption peak. By a process of elimination, it would appear that the final high-energy trapping state is due to hydrogen associated with the lithium-rich T_1 precipitates. This conclusion is supported by the fact that there is a considerably higher fraction of hydrogen trapped at states 5 and 6 for AA2090 in the UA and PA tempers than for the T3 temper (Figure 7), where T_1 is, for the most part, absent (Table II). The T_2 and T_B precipitates have also been identified along high-angle grain boundaries in the UA and PA tempers and may also trap hydrogen. However, only the trapping at T_1 will be referenced in the remainder of this article.

Table III. Calculations of the Binding Energies for the Identified Trapping States; Data for AA2090, UA Temper

Trapping State	$(E_m + E_B)/R$ (K)	$E_m + E_B$ (kJ/mol)	E_B (kJ/mol) (E_B (eV))
Interstitial (state 1)	1810	15.1	0 (0)
Solid solution Li (state 2)	2130	17.7	2.6 (0.0269)
δ' (state 3)	4850	40.3	25.2 (0.261)
Dislocations (state 4)	5630	46.8	31.7 (0.328)
Grain boundaries (state 5 or 6)	—	—	— —
T_1 (state 5 or 6)	—	—	— —

There is no conclusive evidence for the identification of trapping state 1. However, it is believed to be hydrogen associated with interstitial sites in the aluminum matrix. State 1 is of very low energy and, while there may be some contribution from hydrogen adsorbed onto the surface or within a hydrated oxide layer which may not have been accounted for fully, dissolved hydrogen has been measured in defect-free pure aluminum.[41,42] Therefore, some dissolved hydrogen must be present at interstitial sites.

H. *Activation Energies*

Desorption spectra for hydrogen-precharged specimens were generated at four thermal ramp rates varying from 2 °C/min to 15 °C/min. The temperatures at the maximum desorption rates were used to generate Arrhenius plots for each trapping state (Eq. 13). The binding energy of each trapping state was determined (Table III). Due to the uncertainty in fitting states 5 and 6, activation energies for these states were not calculated. In order to determine a binding energy for the trapping states, it was assumed that trapping state 1 corresponds to interstitial hydrogen. Since the activation energy for the desorption of interstitial hydrogen is the migration energy for lattice diffusion, this activation energy has been used to convert the activation energies for desorption (E_a) of the other states to trap binding energies (Table

Table IV. Trap Site Coverage for AA2090, UA Temper.

Desorption State	Trap Identity	Trap Binding Energy E_B (kJ/mol)	Calculated Trap Coverage, θ_T (from Eq. [16])
1[a]	interstitial	0	1.56×10^{-7}
2	Li in solid solution	2.60	4.46×10^{-7}
3	δ'	25.2	4.08×10^{-3}
4	dislocations	31.7	0.0562
5[b]	high angle grain boundaries	35	0.176
6[c]	T_1	38	0.417

[a]The interstitial coverage is calculated from hydrogen content in trapping state 1.

[b]Trapping state 5 will be assumed to be high angle grain boundaries and a binding energy is approximated from the desorption rate data.

[c]Trapping state 6 will be assumed to be T_1 precipitates and a binding energy is approximated from the desorption rate data.

III). Moreover, the activation energy for state 1 is in fairly good agreement with the migration energy of 18.12 kJ/mol, which was determined for an Al-2 wt pct Li binary.[32] If the trapped hydrogen is in equilibrium with the lattice hydrogen, the coverage of each trapping state can be predicted.[49]

$$\frac{\theta_T}{1 - \theta_T} = \theta_L \exp\left(\frac{E_B}{kT}\right) \text{ for } \theta_T < 1 \qquad [14]$$

where θ_T and θ_L are the fractional occupancy of trap and lattice sites, respectively. The calculated coverage for each trapping state is shown in Table IV. The calculated coverage for each trapping state can then be compared to estimates of the trap coverage for each state by approximating the total number of trapping sites for each state.

IV. DISCUSSION

Identification of hydrogen trapping states present in Al-Li-Cu-Zr alloys has been accomplished by comparing hydrogen desorption spectra for alloys of various microstructures with several aging treatments and deformation levels. These observations are supported by the relative binding energies determined for each state. While additional trapping states may be present in other aluminum alloys, six primary trapping states have been observed and identified for the Al-Li-Cu-Zr alloys studied. The desorption of hydrogen from state 1 has been attributed to interstitial hydrogen. The association of hydrogen with interstitial sites is purely attractive in nature,[43] and must result in a fairly low activation energy. Due to the low hydrogen concentration in these alloys (150 wppb or 2.32×10^{17} atoms H/cm^3 in AA2090 using this cathodic charging process) and the high concentration of interstitial sites (6.03×10^{22} sites/cm^3), it is apparent that only a small fraction of the total number of interstitial sites will contain hydrogen. Using the total hydrogen measured in desorption state 1 and the calculated density of available interstitial sites (Appendix A), a coverage of only 1.56×10^{-7} is predicted (Table V).

A. *Solid Solution Lithium*

The addition of lithium to aluminum has been found to increase hydrogen solubility.[32] Therefore, interstitial hydrogen will be attracted to lithium in solid solution. The attraction between interstitial hydrogen and solid-solution lithium will be seen as a binding energy, resulting in an activation energy for hydrogen desorption that is slightly greater than the activation energy for interstitial hydrogen that is not associated with solid-solution lithium. Using a trap binding energy of 2.6 kJ/mol and an interstitial lattice coverage of 1.56×10^{-7}, a trap coverage of 4.46×10^{-7} is calculated for lithium in solid solution (Table IV). This coverage is within an order of magnitude of the trap coverage which is calculated from the total amount of hydrogen desorbed by state 2 (Table V).

B. *δ' Precipitates*

The activation energy for desorption state 3 (δ' precipitates) is less than that for desorption state 4 (dislocations), and is significantly greater than that for interstitial hydrogen. This result is significant because δ' particles, while having a larger lattice constant (more than 6 pct greater) than a pure aluminum matrix, are coherent with the matrix. Therefore, desorption state 3 will be mostly, if not totally, attractive in nature.[43] A trap-site coverage of 4.08×10^{-3} can be calculated using a binding energy of 25.2 kJ/mol. This coverage is just slightly greater than a factor of two higher than the trap coverage determined using the total amount of hydrogen desorbed from trapping state 3 (Table V). To make this assessment, the δ' precipitate density was assumed to be equivalent to that measured by Rioja and co-workers[37] for an Al-2.63Cu-1.73Li-0.12Zr (wt pct) alloy.

C. *Dislocations*

Using a binding energy of 31.7 kJ/mol, a trap coverage of hydrogen at dislocations is calculated to be 0.0562. This is in excellent agreement with the coverage determined from the total hydrogen released by state 4, assuming a dislocation density of 2.86×10^{10} cm/cm^3 for a 6 pct stretch level [37] (Table V).

Hydrogen-dislocation interactions are a very important aspect in the EAC of Al-Li-Cu-Zr alloys. Not only are dislocations a significant physical trapping state for absorbed hydrogen, dislocations can play a major role in the redistribution of absorbed hydrogen during internal hydrogen embrittlement, as well as increase the rate of hydrogen uptake when a material is being plastically deformed in the presence of a hydrogen-bearing environment.

D. *Subgrain Boundaries*

Although dislocations were found to act as sites for hydrogen trapping, there has been no evidence to suggest that subgrain boundaries provide adequate sites for hydrogen trapping. The lack of hydrogen trapping at subgrain sites may be due to the low-energy dislocation structure of a subgrain. Subgrain boundaries consist of dislocations arranged to order their compressive and tensile fields. Therefore, the strain fields of adjacent dislocations partially cancel one another.[44] Because the presence of hydrogen as an atmosphere about an edge dislocation is a result of the compressive and tensile strain fields, the potential cancellation of a portion of these fields may affect hydrogen trapping at these sites. It could be argued that the activation energy of

Table V. Approximate Trap Site Coverage for AA2090, UA Temper

Desorption State	Trap Identity	Trap Density, N_T (Sites/cm^3)[a]	Trapped Hydrogen, C_T (atoms H/cm^3)[b]	Trap Occupancy, $\theta_T = C_T/N_T$
1	interstitial	$6.03 \times 10^{22} = N_L$	$9.46 \times 10^{15} = C_L$	$1.56 \times 10^{-7} = \theta_L$
2	Li in solid solution	4.66×10^{21}	1.92×10^{16}	4.13×10^{-6}
3	δ'	1.35×10^{19}	2.51×10^{16}	1.85×10^{-3}
4	dislocations	1.81×10^{18}	5.14×10^{16}	0.0284
5	high angle grain boundaries	5.92×10^{17}	7.94×10^{16}	0.134
6	T_1	3.34×10^{18}	6.34×10^{16}	0.0190

[a]Determination of trap densities are shown in Appendix A.
[b]Trapped hydrogen concentrations are determined from TDS analysis for the average of three charged (Ni coated and charged for 28 days) specimens.

hydrogen trapped at subgrain boundaries may be very close to the activation energy for another trapping state and may be masked by this other state. However, results of fracture tests for hydrogen-precharged specimens support the conclusion that hydrogen is not trapped at subgrain boundaries.[20,28] The fracture toughness of unrecrystallized AA2090 and recrystallized Al-Li-Cu-Zr alloys containing predissolved hydrogen decreased dramatically when high-angle boundary pathways were favorably oriented for crack growth. However, little effect was observed when subgrain boundary pathways were favorably oriented.

E. *High-Angle Grain Boundaries*

Thermal desorption analysis of the recrystallized alloys has shown that one of the two high-energy trapping states present in Al-Li-Cu-Zr alloys must be high-angle grain boundaries. Since grain boundaries are high-energy defect structures, it stands to reason that high-angle grain boundaries would have a relatively high binding energy. If it is assumed that high-angle grain boundaries are the fifth desorption state and a binding energy of 35 kJ/mol is approximated from the desorption rate spectra, a trap coverage of 0.176 can be calculated. This value is in excellent agreement with the trap coverage calculated from the amount of hydrogen desorbed by state 5 and the available grain-boundary trapping sites for the AA2090 sheet product (0.134, Table V).

F. *T_1 Precipitates*

The AA2090 had a much higher quantity of hydrogen trapped at the two high-energy states when tested in the underaged and peakaged tempers than when specimens in the T3 temper were studied (Figure 7). This is believed to be associated with hydrogen trapping at T_1 particles. While the faces of the T_1 plates provide a coherent interface with the matrix (the {0001} planes of the T_1 phase have a low misfit with the {111} habit planes of the matrix),[45] the edges of these particles produce an interface of high energy. Since T_1 particles are likely to be one of the high-energy trapping states in Al-Li-Cu-Zr alloys, it is proposed that hydrogen will be trapped at the incoherent interfaces of T_1 particles. Assuming T_1 precipitates are the highest energy trapping state and a binding energy of 38 kJ/mol is approximated from the desorption rate spectra, a trap coverage of 0.417 can be calculated. A coverage of 0.019 (Table V) is calculated from the total hydrogen released from state 6. As was the case with the trap occupancy calculations for δ' precipitates, the determination of the trap density for T_1 precipitates was made using data generated by Rioja *et al.*,[37] using an Al-Li-Cu-Zr alloy with a slightly different composition than the AA2090 used in this study.

Globular T_2 ($Al_6Cu(Li,Mg)_3$) and/or T_B (Al_7Cu_4Li) have been observed at high-angle boundaries of the AA2090 alloy in the UA and PA tempers.[46] While no additional trapping states were identified in the PA temper, these precipitates should not be ruled out as potential hydrogen trapping states. The globular precipitates are present in relatively low volume fractions, consequently, identification of hydrogen trapping at these precipitates is difficult.

V. CONCLUSIONS

1. Six hydrogen desorption states have been identified for AA2090. In order of increasing activation energy of desorption, they are interstitial sites, solid solution lithium, δ', dislocations, high-angle grain boundaries, and T_1 precipitates.
2. For the trapping states in which the concentration of available trapping sites is fairly well known (dislocations and high-angle grain boundaries), there is excellent agreement between the trap-site coverage predicted by binding energies and the amount of hydrogen desorbed from each trapping state.
3. Only 4 pct of the total internal hydrogen content is associated with interstitial sites. In contrast, 78 pct of the hydrogen occupies trap states with energies greater than 31.7 kJ/mol.
4. Subgrain boundaries were not found to be a trapping state that could be distinguished from others reported.
5. A high binding energy and, consequently, a large hydrogen coverage at high-angle grain boundary sites was implicated.
6. Dislocations were observed to trap hydrogen in both prestrained and dynamically strained (SET) testing. Hydrogen uptake was enhanced at dislocations by dynamic straining.

ACKNOWLEDGMENTS

This research was supported by NASA–Langley Research Center (D.L. Dicus, project monitor) under the NASA-UVA LA^{2}ST program. Additional funding was provided by the Virginia Center for Innovative Technology and Alcoa Technical Center. The authors thank Peter K. Vandenburgh, Alcoa

Technical Center, for the DSC results and William Benson, UVA, for the TEM results.

APPENDIX
Available trap sites AA2090 UA

A. *High-Angle Grain Boundaries*

Grain Size 4400 × 600 × 10 μm (Table I).

Volume/grain = 2.64×10^7 μm^3 = 2.64×10^{-5} cm^3.

Surface area/grain = 5.38×106 $\mu m^2/2$ = 2.69×10^6 μm^2 = 2.69×10^{14} A^2.

Note that the surface area is divided by 2 since each boundary is the intersection of two grains. For Al a_{rad} = 1.82 A, therefore, a dense-packed surface of Al {111} 5.81×10^{-2} atoms/A^2.

If the entire grain-boundary area were to contain one atom of H/atom Al,

$$2.69 \times 10^{14}\ A^2 \div 2.64 \times 10^{-5}\ cm^3 \times 5.81 \times 10^{-2}\ H\ sites/A^2 = 5.92 \times 10^{17}\ H\ sites/cm^3.$$

B. *Dislocation Trapping*

Rioja *et al.*[37] measured the dislocation density for an Al-2.63Cu-1.73Li-0.12Zr (wt pct) alloy for various stretching levels. For a 6 pct stretch level, dislocation density = 2.86×10^{10} cm/cm^3.

If H atoms are aligned along the tensile side of each dislocation core,

$$1\ H\ site \div 1.58\ A \times (2.86 \times 10^{10}\ cm/cm^3) = 1.81 \times 10^{18}\ H\ sites/cm^3.$$

C. *Available Interstitial Sites*

In the underaged temper, the matrix will become depleted of some of the Li and Cu in solid solution. Therefore, the available interstitial sites will be determined for a pure Al matrix. Density = 2.70 g/cm^3, atomic wt = 26.9815 g/mol ⇒ 6.03×10^{22} atoms Al/cm^3. For fcc metals, there is one octahedral interstitial site/lattice site ⇒ 6.03×10^{22} H sites/cm^3.

Table AI. Effect of Stretching on Measured Dislocation Densities[37]

	As Quenched	
Pct Stretch	Dislocation Density (cm/cm^3)	Foil Thickness (A)
0	5.36×10^8	1480
2	3.04×10^9	2530
6	2.86×10^{10}	1690

D. *Trapping at δ′ Precipitates*

Rioja *et al.*[37] measured the density and size of δ′ precipitates for an Al-2.63Cu-1.73Li-0.12Zr (wt pct) alloy for various aging times at 153 °C. Kilmer[46] examined the AA2090 material used in this study in the UA temper and determined the average δ′ particle to be 80 A in diameter. If the data in Table AII are used and a parabolic coarsening rate is assumed, a particle diameter of 80 A is in very good agreement with the expected diameter for an aging time of 5 hours. At this particle diameter, a density of approximately 116 x 10^{14} ppt/cm^3 would be expected.

If trapping of H is associated with the δ′/matrix interface,

$$\text{area of } \delta' \text{ ppts} = \pi (80\ A)^2 \times 116 \times 10^{14}\ ppt/cm^3 = 2.33 \times 10^{20}\ A^2/cm^3.$$

For a monolayer of H, 5.81×10^{-2} H sites/A^2 (Section A),

$$2.33 \times 10^{20}\ A^2/cm^3 \times 5.81 \times 10^{-2}\ H\ sites/A^2 = 1.35 \times 10^{19}\ H\ sites/cm^3.$$

E. *Trapping at T_1 Precipitates*

Rioja *et al.*[37] measured the density and size of T_1 precipitates for an Al-2.63Cu-1.73Li-0.12Zr (wt pct) alloy for various aging times at 153 °C. Kilmer[46] examined the AA2090 material used in this study in the UA temper and determined the average T_1 precipitate to be 800 A in length. If the data in Table AIII are used and a parabolic coarsening rate is assumed, a particle size of 800 A is in very good agreement with the expected size for an aging time of 5 hours. At this particle size, a density of approximately 33×10^{14} ppt/cm^3 would be expected.

Assume trapping of H is associated with the incoherent interface along the T_1 platelet edges. Total length of incoherent interface = 2 (800 A) = 1600 A/ppt. Therefore,

$$1600\ A/ppt \times 33 \times 10^{14}\ ppt/cm^3 = 5.28 \times 10^{18}\ A/cm^3.$$

For a continuous length of hydrogen along the incoherent interface,

$$0.633\ H\ sites/A \times 5.28 \times 10^{18}\ A/cm^3 \times 0.633\ H\ sites/A = 3.34 \times 10^{18}\ H\ sites/cm^3.$$

F. *Trapping at Li in Solid Solution.*

Assume 1 H atom can be trapped for each Li atom in solid solution. AA2090 is 2.15 wt pct Li and is 2.59 g/cm^3.

Table AII. Densities and Sizes of δ′ Precipitates as a Function of Percent of Stretch and Aging Practice (153 °C)[37]

	2 Hours		16 Hours		72 Hours	
Pct of Stretch	Density ($\times 10^{14}$ ppt/cm^3)	Size (A)	Density ($\times 10^{14}$ ppt/cm^3)	Size (A)	Density ($\times 10^{14}$ ppt/cm^3)	Size (A)
0	729	73.5	33.6	188.5	24.7	381.8
2	255	63.3	48.1	188.6	37.1	356.0
6	171	41.7	45.9	134.0	—	—

Table AIII. Densities and Sizes of T_1 Precipitates as a Function of Percent of Stretch and Aging Practice (153 °C)[37]

	2 Hours		16 Hours		72 Hours	
Pct of Stretch	Density ($\times 10^{14}$ ppt/cm^3)	Size (A)	Density ($\times 10^{14}$ ppt/cm^3)	Size (A)	Density ($\times 10^{14}$ ppt/cm^3)	Size (A)
0	0	0	3.78	1769.2	3.05	2704.5
2	2.78	243.2	17.2	1329.6	8.56	2227.3
6	15.7	668.2	55.6	1045.5	—	—

Therefore, 4.83×10^{21} atoms Li/cm^3. However, some Li has been depleted from solid solution by the precipitation of δ' and T_1. δ' is an $L1_2$-ordered structure (Al_3Li) and is present as 80 A spheres with a density of 116×10^{14} ppt/cm^3. Therefore, 1.89×10^{19} atoms Li in δ'/cm^3.

T_1 is an hcp structure (Al_2CuLi) and is present as 800 A platelets, which are 10 A thick[46] with a density of 33×10^{14} ppt/cm^3. Therefore, 1.56×10^{20} atoms Li in T_1/cm^3. Therefore, approximate Li in solid solution for AA2090-UA is 4.66×10^{21} atoms Li/cm^3. Therefore, 4.66×10^{21} H sites/cm^3.

REFERENCES

1. A. Gray, N.J.H. Holroyd, and W.S. Miller: *1st Int. SAMPE Metals and Metals Processing Conf.*, SAMPE, Covina, CA, 1987, vol. 1, pp. 339-51.
2. E.L. Colvin, S.J. Martha, and R.K. Wyss: *Aluminum Alloys—Physical and Mechanical Properties*, EMAS Ltd., London, 1986, vol. 3, pp. 1853-67.
3. R.G. Buchheit and G.E. Stoner: *Aluminum Lithium Alloys V*, MCE Publications Ltd., Birmingham, United Kingdom, 1989, pp. 1347-56.
4. J.P. Moran, R.G. Buchheit, and G.E. Stoner: *Parkins Symp. on Fundamental Aspects of Stress Corrosion Cracking*, TMS, Warrendale, PA, 1992, pp. 159-70.
5. E.I. Meletis: *Parkins Symp. on Fundamental Aspects of Stress Corrosion Cracking*, TMS, Warrendale, PA, 1992, pp. 353-70.
6. R.G. Buchheit, Jr., J.P. Moran, and G.E. Stoner: *Corrosion*, 1990, vol. 46, pp. 610-17.
7. E.I. Meletis and W. Huang: *Mater. Sci. Eng. A*, 1991, vol. A148, pp. 197-209.
8. R. Balasubramaniam, D.J. Duquette, and K. Rajan: *Acta Metall.*, 1991, vol. 39, pp. 2597-2605.
9. R. Balasubramaniam, D.J. Duquette, and K. Rajan: *Acta Metall.*, 1991, vol. 39, pp. 2607-13.
10. C. Kumai, J. Kusinski, G. Thomas, and T.M. Devine: *Corrosion*, 1989, vol. 45, pp. 294-302.
11. R.S. Piascik and R.P. Gangloff: *Metall. Trans. A*, 1991, vol. 22A, pp. 2415-28.
12. G. Ehrlich: *J. Phys. Chem.*, 1956, vol. 60, pp. 1388-1400.
13. P.A. Redhead: *Vacuum*, 1962, vol. 12, pp. 203-11.
14. G. Carter: *Vacuum*, 1962, vol. 12, pp. 245-54.
15. J.Y. Lee, J.L. Lee, and W.Y. Choo: *Current Solutions to Hydrogen Problems in Steels*, ASM, Metals Park, OH, 1982, pp. 423-27.
16. E.V. Kornelsen and A.A. van Gorkum: *Vacuum*, 1981, vol. 31, pp. 99-111.
17. P.N. Anyalebechi: *Light Metals 1991*, TMS, Warrendale, PA, 1991, pp. 1025-46.
18. G.M. Pressouyre and I.M. Bernstein: *Metall. Trans. A*, 1981, vol. 12A, pp. 835-44.
19. M. Iino: *Acta Metall.*, 1982, vol. 30, pp. 367-75.
20. S.W. Smith and J.R. Scully: *Hydrogen Effects in Materials*, TMS, Warrendale, PA, 1996, pp. 131-40.
21. *ASM Specialty Handbook, Aluminum and Aluminum Alloys*, J.R. Davis, ed.; ASM INTERNATIONAL, Materials Park, OH, 1993, pp. 121-42.
22. J.A. Wert, N.E. Paton, C.H. Hamilton, and M.H. Mahoney: *Metall. Trans. A*, 1981, vol. 12A, pp. 1267-76.
23. J. White, W.S. Miller, I.G. Palmer, R. Davis, and T.S. Saini: *Aluminum-Lithium III*, Institute of Metals, London, 1985, pp. 530-38.
24. A. Csanady, K. Papp, and E. Pasztor: *Mater. Sci. Eng.*, 1981, vol. 48, pp. 35-39.
25. K. Papp and E. Kovacs-Cseteni: *Scrip. Metall.*, 1981, vol. 15, pp. 161-64.
26. T. Ishikawa and R.B. McLellan: *Acta Metall.*, 1986, vol. 34 (6), pp. 1091-95.
27. J. Albrecht, I.M. Bernstein, and A.W. Thompson: *Metall. Trans. A*, 1982, vol. 13A, pp. 811-20.
28. S.W. Smith: Ph.D. Dissertation, University of Virginia, Charlottesville, VA, 1995.
29. D.P. Woodruff and T.A. Delchar: *Modern Techniques of Surface Science*, Cambridge University Press, Cambridge, United Kingdom, 1986, pp. 279-99.
30. K. Ono and M. Meshii: *Acta Metall.*, 1992, vol. 40, pp. 1357-64.
31. R.A. Outlaw, D.T. Peterson, and F.A. Schmidt: *Metall. Trans. A*, 1981, vol. 12A, pp. 1809-60.
32. P.N. Anyalebechi: *Metall. Trans. B*, 1990, vol. 21B, pp. 649-54.
33. H.E. Kissinger: *Anal. Chem.*, 1957, vol. 29, pp. 1702-06.
34. P.N. Anyalebechi: Alcoa Technical Center, Alcoa Center, PA, unpublished research, 1994.
35. P.N. Anyalebechi: *Light-Weight Alloys for Aerospace Applications*, TMS, Warrendale, PA, 1989, pp. 249-68.
36. W.S. Miller, J. White, and D.J. Lloyd: *Aluminum Alloys—Physical and Mechanical Properties*, EMAS Ltd., London, 1986, pp. 1799-1836.
37. R.J. Rioja, P.E. Bretz, R.R. Sawtell, W.H. Hunt, and E.A. Ludwicjak: *Aluminum Alloys—Physical and Mechanical Properties*, EMAS Ltd., London, 1986, pp. 1781-97.
38. K.V. Jata and E.A. Starke, Jr.: *Metall. Trans. A*, 1986, vol. 17A, pp. 1011-26.
39. J.M. Papazian: *Thermal Analysis in Metallurgy*, TMS, Warrendale, PA, 1992, pp. 259-78.
40. H.K. Birnbaum, C. Buckley, F. Zeides, E. Sirois, P. Rozenak, S. Spooner, and J.S. Lin: *J. Alloys Compds.*, 1997, vols. 253–254, pp. 260-64.
41. C.E. Ransley and H. Neufeld: *J. Inst. Met.*, 1948, vol. 74, pp. 599-620.
42. R. Edwards and W. von Eichenauer: *Scrip. Metall.*, 1980, vol. 14, pp. 971-73.
43. G.M. Pressouyre: *Metall. Trans. A*, 1979, vol. 10A, pp. 1571-73.
44. R.E. Reed-Hill: *Physical Metallurgy Principles*, 2nd ed., PWS Engineering, Boston, MA, 1973, pp. 274-77.
45. R.J. Rioja and E.A. Ludwiczak: *Proc. 3rd Int. Al-Li Conf.*, Oxford, United Kingdom, 1985, pp. 471-82.
46. R.J. Kilmer: Ph.D. Dissertation, University of Virginia, Charlottesville, VA, 1994.
47. C.P. Blankenship, Jr., E. Hornbogen, and E.A. Starke, Jr.: *Mater. Sci. Eng. A*, 1993, vol. A169, pp. 33-41.
48. A. Turnbull, R.B. Hutchings, and D.H. Ferriss: *Mater. Sci. Eng. A*, 1997, vol. A238, pp. 317-28.
49. R.A. Oriani: *Acta Metall.*, 1970, vol. 18, pp. 147-57.